Chapter 6

Investigating the carbon cycle

In this chapter, the models and techniques described in the previous three chapters are used together to investigate features in the Law Dome CO_2 and $\delta^{13}C$ ice core record. The ice core record provides an opportunity to estimate the isofluxes arising from the disequilibrium between the atmosphere and the oceans and biosphere due to industrial CO_2 emissions. A review of previous isoflux estimates and discussion of the impact of the isoflux on net CO_2 fluxes calculated by a double deconvolution is given. This is followed by discussion of the Kalman filter double deconvolution results. Natural variability on the century and decadal time scale are investigated by comparing the results from the forward, single and double deconvolution calculations. Detailed investigation of the CO_2 flattening around the 1940s is given. The anthropogenic trend in $\delta^{13}C$ is then discussed.

6.1 Isofluxes

The global isoflux (isotopic disequilibrium flux) is required for solving the ^{13}C budget for net CO_2 fluxes, yet it is very difficult to estimate from direct measurements (see Section 2.5). There have been a number of different estimates for the oceanic, biospheric and total isoflux using a range of methods. Figure 6.1 shows many of these, including the estimate from the BDM single deconvolution. Some estimates are given as an average value over a number of years, others vary with time. The different estimates (roughly in the order in which they were published) were obtained as follows. The Quay et al. (1992) isoflux estimate for the biota ('Quay') is based on an NPP of 60 GtC y^{-1} and an isotopic disequilibrium of 0.2 ‰. This isoflux estimate is significantly lower than subsequent estimates. The Tans et al. (1993) ocean isoflux estimate ('Tans') is based on

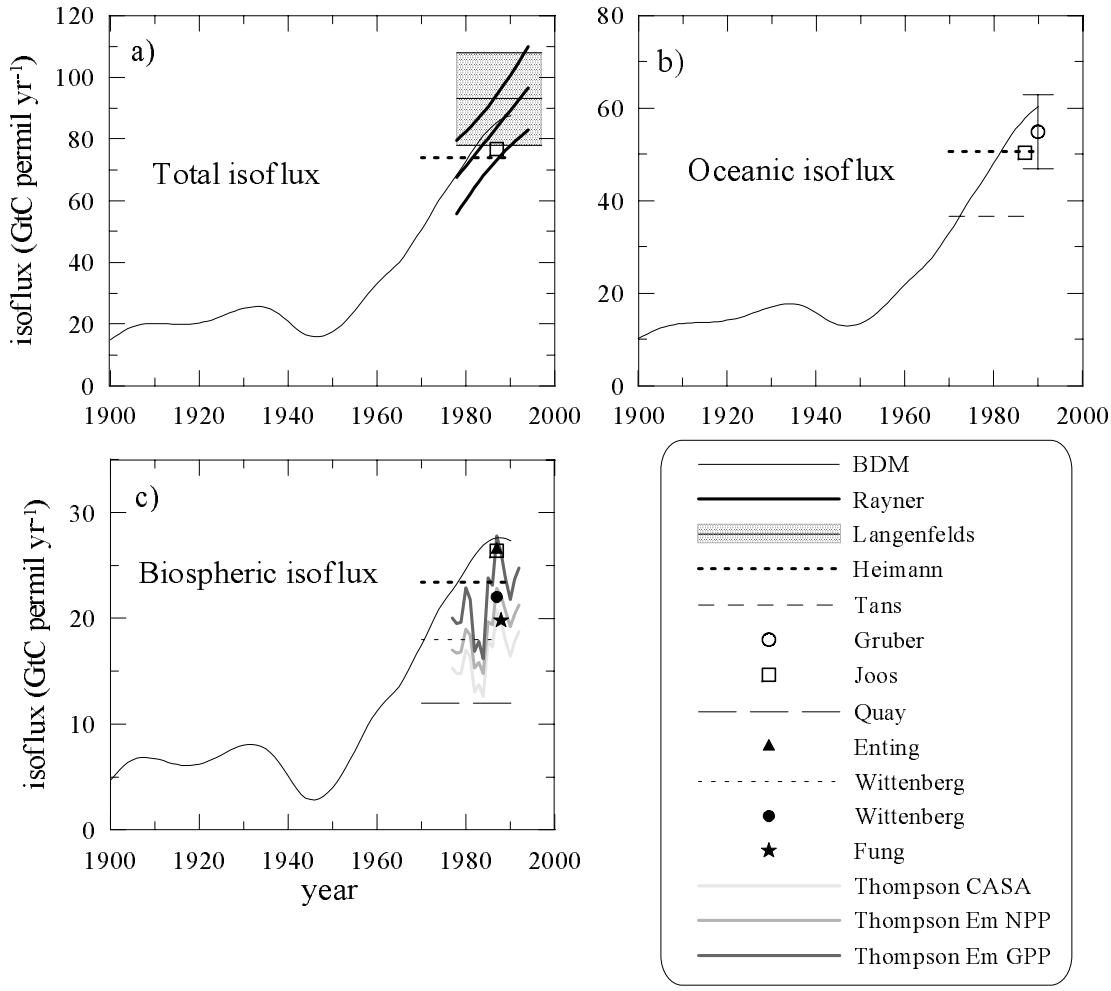

Figure 6.1: Isotopic disequilibrium flux from the BDM compared with a range of other estimates (see text for details).

the measured disequilibrium between the ocean surface and the atmosphere. Enting et al. (1993) estimated the biota isoflux ('Enting') with the Emanuel et al. (1981) biospheric model and the Siple ice core record of δ^{13}C. The Heimann and Maier-Reimer (1996) values ('Heimann') are from their consistent scenario, and are very similar to the BDM values at the corresponding time.

Fung et al. (1997) estimated with a biospheric process model a global disequilibrium of 0.33 ‰ for 1988, which when multiplied by 60 GtC y^{-1} gives the value ('Fung') shown in the figure. Wittenberg and Esser (1997) estimated the biota isoflux ('Wittenberg') using a high-resolution biosphere model and the Siple δ^{13}C ice core record. Values are

given for 1987 and for the period 1970–1987. Joos and Bruno (1998) estimated the ocean and biota isofluxes ('Joos') for their double deconvolution using the HILDA ocean model and a 4-box biosphere model. Gruber et al. (1999) estimated the ocean isoflux ('Gruber') from new high-quality global surface ocean measurements. Their value is significantly higher than the Tans measurement-based estimate. It applies for a later time, although the difference between the two values is larger than the change in the BDM estimate for the corresponding times.

Langenfelds et al. (1999) estimated the total isoflux ('Langenfelds') that made the ^{13}C budget consistent with their budget based on the 19-year trend in atmospheric O_2 from the Cape Grim Air Archive. Shading in the figure indicates the uncertainties on their estimate. Rayner et al. (1999a) estimated the total isoflux and uncertainties ('Rayner') by using the same O_2 data in their space-time synthesis inversion. They determined a mean value and linear trend for the isoflux, in contrast to many of the other estimates which are a single number. The uncertainty on their estimate is greatest at the beginning and end of the time interval. The Rayner et al. (1999a) estimate is in very good agreement with both the mean value and the slope of the BDM estimate. The agreement between these two independent isoflux estimates (i.e. 'Rayner' and 'BDM') was described by Francey et al. (1999c). (The two O_2 results ('Rayner' and 'Langenfelds') differ slightly because of different assumptions and methods used in the calculations.)

Thompson and Randerson (1999) estimated the biota isoflux using impulse response functions of the Emanuel et al. (1981) box model of the biosphere and the CASA biosphere model, which is a spatially explicit NPP and soil carbon biogeochemistry model ('Thompson CASA'). The Emanuel model is run as NPP-referenced ('Thompson Em NPP') and GPP-referenced ('Thompson Em GPP'), i.e. using either NPP or GPP as the carbon input from the atmosphere (see Thompson and Randerson (1999)). (The GPP-referenced calculation considers the effect of autotrophic respired carbon, which is slightly older than atmospheric carbon and therefore contributes to the isoflux, giving a higher isoflux than the NPP-referenced calculation.) The Thompson and Randerson isoflux estimates have significant interannual variability due to the large variability in the atmospheric $\delta^{13}C$ record that they used. Variations in atmospheric $\delta^{13}C$ are mirrored in the disequilibrium, because they are not matched by variations in biospheric $\delta^{13}C$ on the interannual time

scale. The other estimates in Figure 6.1 either used smoothed estimates of atmospheric $\delta^{13}C$ or estimated a mean value or linear function for the isoflux, and therefore did not have this effect. Thompson and Randerson suggested that the high interannual variability in the isoflux may impact inversion calculations.

The isoflux arises mainly because of the decreasing $\delta^{13}C$ in the atmosphere due to anthropogenic sources. However, other factors (such as the C_3 to C_4 conversion, temperature changes) will also affect the isotopic disequilibrium. This will account for a small fraction of the variation between the estimates shown in Figure 6.1, as some are based on measurements, others on models that include only anthropogenic inputs. The range covered by the different isoflux estimates in Figure 6.1 is significant. It will explain some of the variation in net CO_2 flux estimates from different studies based on the ^{13}C budget.

The $\delta^{13}C$ record used by Thompson and Randerson (1999) in their isoflux calculation (which is described as aggregate atmospheric data from Francey et al. (1995b)) has significantly greater interannual variability than the Cape Grim record of Francey et al. (1995b), possibly due to matching records from different latitudes without correcting for spatial gradients. The interannual variability in their biota isoflux estimate is therefore probably an over-estimate. The BDM's 2-box biosphere model (which has parameters tuned to match the response function of the Emanuel et al. (1981) model) with Thompson and Randerson's $\delta^{13}C$ record gives about the same variation in the isoflux as their GPP-referenced Emanuel model. The range in the isoflux values determined using the Cape Grim $\delta^{13}C$ data from Francey et al. (1995b) in the 2-box model is about a factor of 2 smaller than using the record used by Thompson and Randerson. Although the interannual variability in the biota isoflux for the Cape Grim record is less than suggested by Thompson and Randerson, the effect is also seen in the ocean isoflux and it may still be important for inversions.

The effect of this kind of variation in the estimated isoflux on inversion of CO_2 and $\delta^{13}C$ for net fluxes can be tested using the double deconvolution calculation of Francey et al. (1995b). Francey et al. used the biota isoflux calculated by Enting et al. (1993) with a linear trend (dashed line in Figure 6.2d) and the Tans et al. (1993) measurement-based ocean isoflux estimate, with a linear trend determined with an ocean box model (dashed line in Figure 6.2c). The dashed lines in Figures 6.2a and 6.2b show the net fluxes

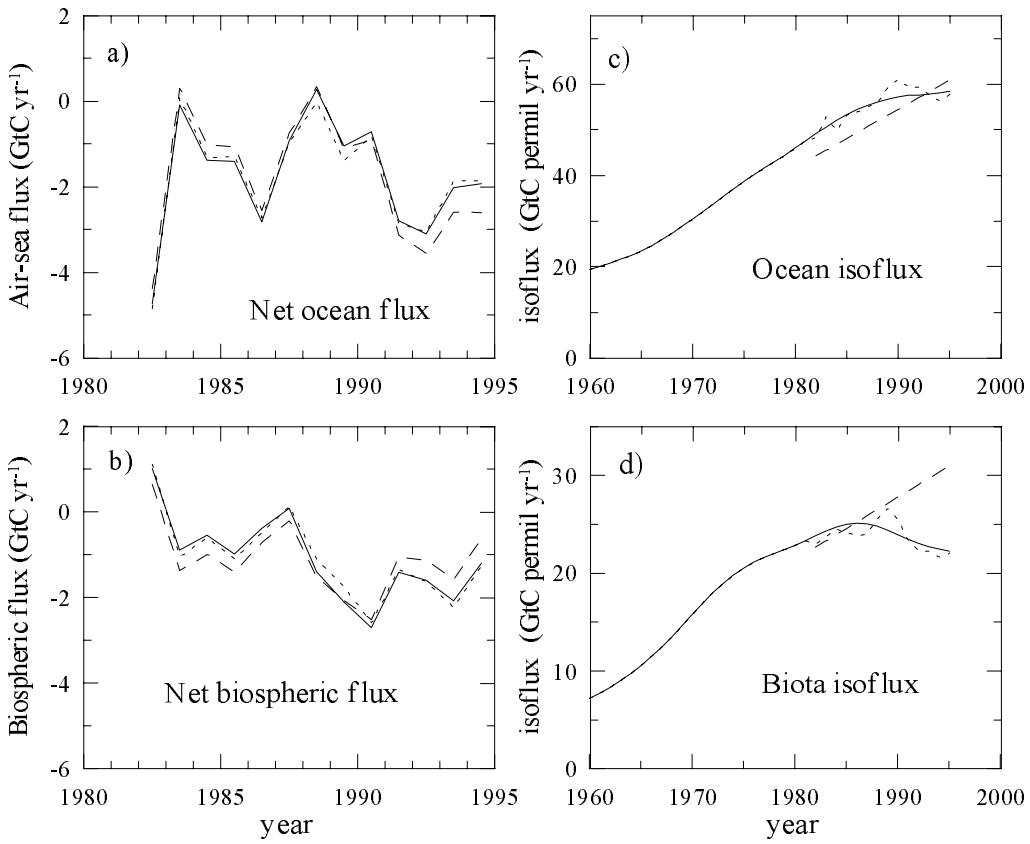

Figure 6.2: a) Oceanic and b) biospheric net fluxes from a mass balance double deconvolution calculation using the CO_2 and $\delta^{13}C$ data from Francey et al. (1995b). The deduced fluxes in a) and b) are calculated using the isofluxes with the corresponding line styles in c) and d). The dashed lines show the isofluxes used by Francey et al. (1995b), and the net fluxes calculated with these isofluxes are essentially the same as those from Francey et al. (1995b). The solid and dotted lines show the isofluxes determined using a smooth spline and the annual $\delta^{13}C$ data from Francey et al. (1995b), respectively.

calculated with these isofluxes in a mass balance double deconvolution (Section 2.10) using the global CO_2 record from Conway et al. (1994) and the Cape Grim $\delta^{13}C$ record. (The CO_2 and $\delta^{13}C$ is the same as that used by Francey et al., but the fluxes differ slightly from the Francey et al. solution due to the use of more recent estimates of the fossil source and its isotopic signature.) Figures 6.2c and 6.2d show isofluxes estimated with smooth spline fits to the CO_2 and $\delta^{13}C$ ice core records (solid line) and also with the annual CO_2 and $\delta^{13}C$ values of Francey et al. (1995b) after 1982 (dotted line). These isofluxes are calculated with a double deconvolution performed essentially as in Joos and Bruno (1998), with a mixed layer response function representation of the BDM ocean model and

the BDM 2-box biosphere model. The Francey et al. biota isoflux is similar to the BDM estimate in the mid eighties, but continues to increase while the BDM estimate decreases. Their ocean isoflux is slightly lower than the BDM estimate in the eighties.

Figures 6.2a and 6.2b show the net fluxes calculated with the same CO_2 and $\delta^{13}C$ data as used by Francey et al. (1995b), but with the three different sets of isoflux estimates shown in Figures 6.2c and 6.2d. The total isoflux used by Francey et al. is lower than the BDM values before 1989 and higher after, causing lower ocean uptake before 1989 and higher uptake after. The differences in partitioning due to year-to-year variability in isoflux from atmospheric $\delta^{13}C$ variations (comparing the dotted and solid lines) are fairly small when compared with the variability in the net fluxes estimated from this data. The difference is greatest (about 0.35 GtC y^{-1}) in 1989, while the range of the net oceanic flux from this calculation is about 4 GtC y^{-1}. However, as mentioned in Section 2.4, interannual variability in the air-sea flux as determined by ocean models and measurements is generally much less than that seen in atmospheric CO_2 growth rates and estimated by Francey et al. (1995b). The effect of the interannual variability in isoflux on partitioning may well be important if the air-sea flux variations (and other drivers of the isoflux to be described shortly) are in fact small.

Figure 6.3 shows a calculation that uses the estimated global ocean net fluxes from Le Quéré et al. (2000) (dashed line and symbols in Figure 6.3a) and global biospheric net fluxes from the CASA biosphere model (Friedlingstein et al., 1997) (dashed line and symbols in 6.3b). These fluxes were run forward in the BDM to generate CO_2 and $\delta^{13}C$ time series, which were then inverted with the mass balance double deconvolution using different isofluxes. (The oceanic and biospheric fluxes have each been shifted by a constant amount so that the 1980–1995 means are the same as for the fluxes from the splines to avoid a sudden shift.) Figures 6.3c and 6.3d show the isofluxes calculated using the same smooth CO_2 and $\delta^{13}C$ splines as in Figures 6.2c and 6.2d (solid lines) and using the generated CO_2 and $\delta^{13}C$ data (dotted lines). Inversion with the interannually varying isofluxes gives the input fluxes (as expected) but inversion with the spline isofluxes gives the fluxes shown in Figures 6.3a and 6.3b by the solid lines. The errors due to neglecting interannual variations in isofluxes are greater than the interannual variability in the air-sea flux calculated by Le Quéré et al. (2000). Fortunately this isoflux variability is fairly

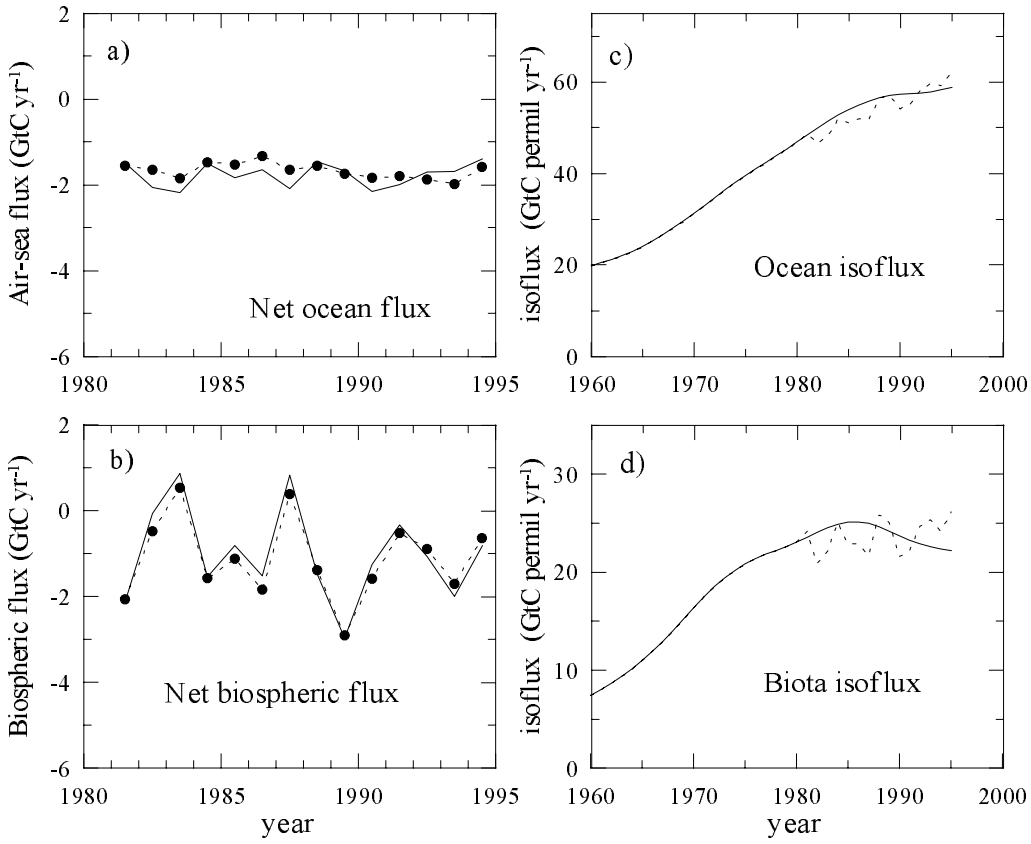

Figure 6.3: a) Dotted line and symbols show the oceanic net flux from Le Quéré et al. (2000). Solid line shows fluxes calculated by inverting with the spline isofluxes. b) Dotted line and symbols show the biospheric net fluxes from the CASA model (Friedlingstein et al., 1997). Solid line shows fluxes calculated by inverting with the spline isofluxes. c) Ocean and d) biosphere isofluxes calculated with the splines (solid line) and the generated data (dotted lines).

easily calculated as long as the need is recognised. It is only a problem when a constant or smoothly varying isoflux is used, as has generally been the case in the past. As suggested by Thompson and Randerson (1999), response functions are a cheap, convenient way to model this variation.

There are other processes that may cause interannual variations in isoflux that are not as easy to predict as those already discussed. For example, variations in sea surface temperature (which will affect isotopic fractionation) or wind speed or sea-ice coverage (which will affect gross exchange of CO_2) in the Southern Ocean may cause significant variation in the ocean isoflux. It should be possible to quantify these effects, as the

relevant data exist. Another possibility is that variations in ocean circulation may impact atmospheric δ^{13}C, but this may not be so easy to quantify. More work is needed in this area, because if these effects do cause significant variations in atmospheric δ^{13}C, then this must be known for the δ^{13}C budget. The critical point here is to distinguish δ^{13}C variations that are associated with net CO_2 fluxes, from those that are not (i.e. the isofluxes). Currently, δ^{13}C variations are interpreted in terms of net CO_2 fluxes, apart from the smoothly varying isofluxes. Quantifying the effects suggested above will require analysis of spatial distributions (of the CO_2 flux, temperature, wind speed etc.), and will not be covered in this thesis. On the decadal and century time scales in the Law Dome ice core record, it is reasonable to assume that spatial mixing and temporal averaging will remove these effects, even if they are significant locally at short time scales. Even on the interannual time scale, large coherent regions would probably need to be involved to influence global δ^{13}C levels.

It is possible that there is significant interannual variation in the biota isoflux as a result of the conversion of C_3 forests to C_4 pastures due to land-use change. Following a disturbance, carbon is fixed with the weaker C_4 discrimination but respiration from the soil pool has the isotopic signature of carbon fixed with the strong C_3 discrimination. This may cause a large isoflux. However, Ciais et al. (1999) estimated that the conversion of C_3 forests to C_4 pastures due to land-use change contributes only 4 GtC ‰ y^{-1} to the global isoflux. This estimate, which is based on a residence time for the biosphere of 15 years, gives the total isoflux due to C_3 to C_4 conversion. Spatial averaging may mean that interannual variability is considerably smaller than this, particularly when expressed in terms of the resultant variation in the net flux partition, although it needs to be quantified.

Variation in the isoflux over time scales of decades to centuries depends on the residence times of carbon in the biosphere and ocean. Partitioning CO_2 uptake over a decade into oceanic and biospheric components with ^{13}C requires the average isoflux for the period. To give an indication of the sensitivity of the ocean isoflux to model structure without the effect of different atmospheric records, Figure 6.4 shows isofluxes calculated with mixed layer pulse response functions for 4 different ocean models (Joos et al., 1996) and for the BDM, each used in a mass balance double deconvolution. The total isoflux from the single deconvolution in the BDM is also shown. The same biosphere model is used in

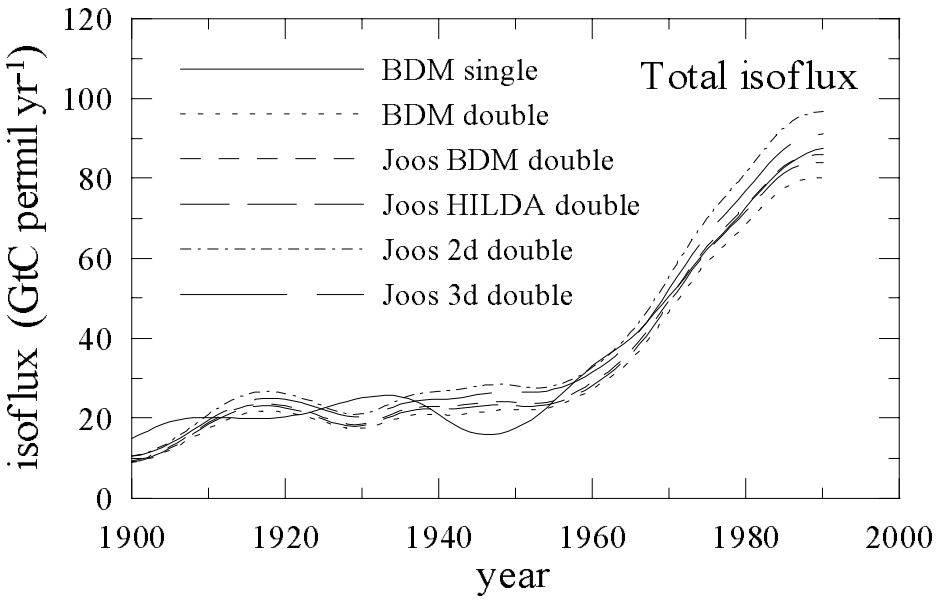

Figure 6.4: Total isoflux calculated by the BDM for single and double deconvolution calculations, and by double deconvolution using mixed layer pulse response functions from Joos et al. (1996) for 4 different ocean models. The same biosphere model (the BDM's 2-box model) is used in all calculations.

all calculations. There is a range of about 17 GtC ‰ yr^{-1} in the 1990 ocean isoflux estimates, with about 13 GtC ‰ yr^{-1} for just the 4 Joos et al. (1996) models. The net CO_2 flux partitioning with the isofluxes from the 4 Joos et al. ocean models in the double deconvolution has a range of about 0.8 GtC yr^{-1}, which is as expected from the isoflux range (i.e. $\delta I/16$, see Section 2.5). Joos and Bruno (1998) performed the same sensitivity test in their double deconvolution, giving the results in terms of ocean uptake. They found a range of about 0.5 GtC yr^{-1} in the 1990 ocean uptake from their 4 ocean models. This is less than the range found here, presumably due to the use of slightly different fractionation factors and different atmospheric histories.

A simple, 1-box biosphere model can be used to test what it is that most influences the calculated isoflux in a model. Consider a 1-box biosphere of size S GtC and with a gross flux between it and the atmosphere of F GtC yr^{-1}. A measure of the turnover time for the biosphere box is then S/F yr. The isotopic disequilibrium and isoflux in 1990 are calculated with this simple model by tracking the ice core $\delta^{13}C$ record. F and S are held constant for a single integration, but different values can be used to test the sensitivity of

the disequilibrium and isoflux to these values. If F is increased by 20 % (which decreases the turnover time), the disequilibrium decreases by 12 % and the isoflux increases by only 6 %. If S is increased by 20 % (increasing the turnover time), both the disequilibrium and the isoflux are increased by 12 %. If both F and S are increased by 20 %, there is no change in the disequilibrium but the isoflux increases by 20 %. For the ^{13}C budget in a double deconvolution, it is the isoflux, not the disequilibrium that matters. The disequilibrium is sensitive to the turnover time of the biosphere, but it doesn't matter whether this is altered by changing F or S. The isoflux is sensitive to the turnover time and the gross flux. If the turnover time is changed by altering F, there is some compensation for the isoflux, giving a smaller change than if the turnover were changed by altering S. This occurs because the isoflux is the product of F and the disequilibrium, and increasing F decreases the disequilibrium. This means that the size of the reservoirs in a model have a stronger impact on the isoflux than the gross flux.

The BDM's 2-box biosphere model, with a 20 % change in all fluxes and/or the size of both boxes gives very similar variation. These results should apply at least broadly to more complex models of the biosphere. It is likely that there is also some compensation for the ocean isoflux with different gross fluxes. This is good, as Joos and Bruno (1998) found that most of the range in isoflux for their 4 ocean models was due to different gas exchange coefficients, rather than ocean transport, in the models.

Randerson et al. (1999) noted that the mean residence time of a biosphere model affects both the estimated isotopic disequilibrium (which affects partitioning and therefore estimation of the biospheric uptake) and carbon storage in response to NPP stimulation by elevated atmospheric CO_2 levels (CO_2 fertilisation). A higher mean residence time in a model suggests lower biospheric uptake via the isotopic disequilibrium in an inversion, but greater biospheric uptake for a given increase in NPP due to CO_2 fertilisation. Randerson et al. tested the consistency of the two estimates of biospheric uptake in the CASA biosphere model. They found the mean residence time above which total uptake from CO_2 fertilisation would exceed the ^{13}C-based estimate of the land sink, and can therefore put an upper bound on the biospheric isoflux. Their upper bound of 29 years mean residence time, corresponding to about 25 GtC ‰ y^{-1} for the biospheric isoflux uses a fairly low ocean isoflux value (based on Tans et al. (1993)). A higher ocean isoflux would reduce the

upper bound on the mean residence time and the isoflux. The Randerson et al. results should depend on how the mean residence time is varied (i.e. by changing fluxes or reservoir sizes). The disequilibrium does depend in a simple way on the mean residence time, but the isoflux, and therefore the deduced fluxes, are more complicated.

In summary, isofluxes are the key to using $\delta^{13}C$ and CO_2 to infer net CO_2 fluxes, and although there are some uncertainties they can be reasonably well determined. For inversions on interannual time scales, it is best to use atmospheric $\delta^{13}C$ variations for calculating the isofluxes, as these variations are not mirrored in the biosphere or ocean, and this can cause variability in the isofluxes. This will mainly be important for inversions if interannual variability in the ocean CO_2 flux is small, as suggested by ocean models and measurements. It has always been assumed that variability in the ocean isoflux due to variation in temperature, wind speed, sea ice extent and ocean circulation is negligible. This is a reasonable assumption, but needs to be tested. For biospheric models, and probably also for oceanic models, there is greater uncertainty in the calculated disequilibrium than in the isoflux, due to uncertainties in the gross flux. Uncertainty in the model reservoir size contributes to both the disequilibrium and isoflux. Uncertainty in the long term isoflux due to using different ocean models translates into an uncertainty of about 0.8 GtC y^{-1} in the net fluxes in 1990. This uncertainty is largest for recent decades. Before 1950 the isoflux range from the different ocean models leads to less than 0.4 GtC yr^{-1} uncertainty in net flux.

6.2 Discussion of double deconvolution results

The standard Kalman filter double deconvolution calculation for the pre-industrial period, DD3, is shown in Figure 5.18. The value of $\mathbf{Q}$ used in the random walk model for this calculation allows a source change of about 0.3 GtC y^{-1} over 100 years. This gives less smoothing than in the Joos et al. (1999) double deconvolution on the same ice core record, which uses a spline fit with a cut-off period of about 300 years in the pre-industrial. The main feature in the ice core record during the pre-industrial period is the LIA. The CO_2 measurements define the LIA quite well, but $\delta^{13}C$ is rather sparse. As has already been mentioned, $\delta^{13}C$ was higher during the LIA than at other times. The Kalman filter and the Joos et al. (1999) results both suggest biospheric uptake as well as an oceanic source for the

LIA period. It is not known whether $\delta^{13}C$ increased at the same time as CO_2 decreased. The Ce96 sponge record of Böhm et al. (2000) in Figure 4.13 shows almost linear $\delta^{13}C$ increase between about 1550 and 1670. The mixed layer $\delta^{13}C$ might be expected to lag behind the atmospheric signal for features caused by the land biosphere, and also to be smoothed in time.

Two standard calculations of the Kalman filter double deconvolution using the smoothing suggested by the firn model were identified in the previous chapter. One uses data uncertainties that could be described as optimistic (DD1) and the other uses more conservative data uncertainties (DD2). These calculations resolve decadal variations and will be useful for studying the industrial period. The Joos et al. (1999) double deconvolution on the same ice core data gives sources that are a little more smoothed than the DD2 case due to their choice of smoothing for the splines (40 year cutoff period). The **Q** in the Kalman filter allows source changes of about 1 GtC y^{-1} in 10 years in the random walk model. In general, many of the variations in both biospheric and oceanic fluxes in the Kalman filter calculations and the Joos et al. (1999) study correspond. Decadal scale variability has a larger amplitude in the DD1 than the DD2 calculation. A KFDD calculation focusing on the 1940s flattening will be described in Section 6.4. The 1940s flattening is not very pronounced in the two standard calculations because DSS data that doesn't show the flattening is included in the calculation.

The Kalman filter double deconvolution calculations (both ARF and MLRF, but not the very smooth DD3 calculation) have large anticorrelated peaks in the biospheric and oceanic fluxes between about 1800 and 1850. The DE08 and DE08-2 records began in this period, so there is a change in the time resolution of the measurements due to the different firn smoothing at DSS and DE08/DE08-2. Perhaps more importantly, there is also a change in the data density at this time, particularly for $\delta^{13}C$. Figure 6.5 shows the DD1 double deconvolution results and the ice core measurements with the DE08, DE08-2 and DSS measurements distinguished. The Joos et al. (1999) calculation, with 300 year spline cutoff, does not show this behaviour. However, a mass balance double deconvolution using the splines to the Law Dome record described in previous chapters does show a similar anticorrelated peak.

It is not clear from the ice core measurements how CO_2 and $\delta^{13}C$ might have actually

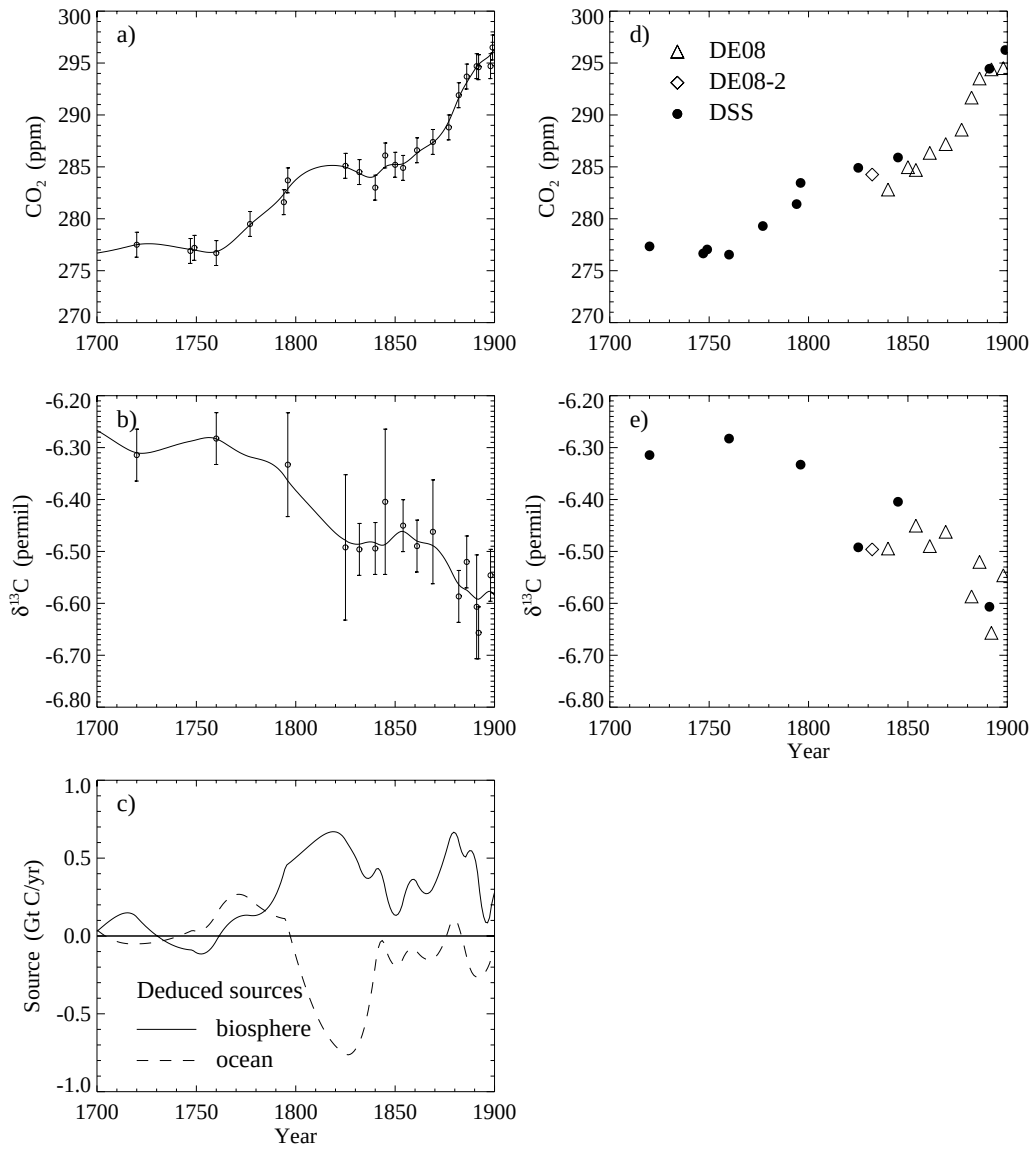

Figure 6.5: a) CO_2 concentration, b) $\delta^{13}C$ and c) deduced sources from the Kalman filter double deconvolution (DD1) with mixed layer pulse response functions around the beginning of the DE08 and DE08-2 records. Ice core measurements of d) CO_2 and e) $\delta^{13}C$ are shown with different symbols for the three different ice cores.

varied around this time. There are three measurements, one from each of the three cores, that are consecutive and close together in time (dated 1825, 1832 and 1840) with very similar δ^{13}C but different CO_2. This type of variation is possible, as oceanic exchange affects CO_2 with little effect on δ^{13}C. However, the fact that the three measurements are within 15 years, and smoothing on the ice core measurements is around 10–20 years may indicate a problem with one or more of these data points. If the δ^{13}C of these 3 measurements is not used in the inversion, then the fluxes calculated for this time are quite different, and the strong peaks disappear. The different smoothing at DSS compared to DE08/DE08-2 may slightly confuse the picture, perhaps with features in the DE08/DE08-2 record not being seen at DSS, similar to what is thought to have occurred for the 1940s flattening. However, removing the DSS points at 1825 and 1845 from the calculation barely alters the deduced fluxes.

Other information may be useful here. The H15 CO_2 ice core record (Figure 2.8c) has a suggestion of a decrease in CO_2 after 1800, following the initial increase which is probably the return from the LIA. The Siple CO_2 ice core record (Figure 2.8a) has one measurement that may also suggest this. The H15 and Siple δ^{13}C ice core records (Figure 2.8b and 2.8d) are very scattered, so are difficult to interpret. There is some evidence in the δ^{13}C sponge records of Böhm et al. (2000) that δ^{13}C decreased until about 1800, then increased for perhaps 40 years, then began the industrial decrease (Figure 4.13). Dating of the sponge records may not be exact, so features in the sponge record may be slightly shifted relative to the ice core record. Fossil fuel emissions before 1850 are expected to have been negligible (Marland et al., 1999) and the source due to land-use change was probably less than 0.5 GtC y^{-1} and increasing quite smoothly. The only estimates for land-use change prior to 1850 published by Houghton are for the U.S. (Figure 2.12c). They show a small step change around 1800, then a gradual increase to less than 0.2 GtC y^{-1} in 1850. There is evidence in climate records of a return to the colder LIA conditions in the 19^{th} century (Figure 2.13). While the large anticorrelated peaks suggested by the double deconvolution are unlikely to be real, there is evidence in the δ^{13}C sponge records as well as the ice core records that CO_2 variation after 1800 may have been more complicated than a simple, smooth transition into the industrial period. Climate is more likely to have been responsible than anthropogenic fluxes, unless there are significant errors in the

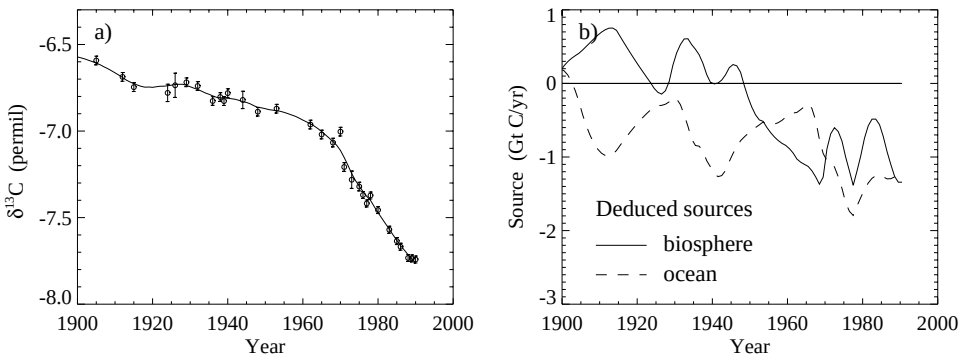

Figure 6.6: a) δ^{13}C and b) deduced sources from the Kalman filter double deconvolution with the 1970 δ^{13}C outlier used in the model. The data uncertainties and **Q** are as in DD1.

estimates of the anthropogenic fluxes. New ice core measurements should provide better insight into the carbon cycle around this time.

Two Law Dome δ^{13}C measurements (dated 1969.7 and 1970.2) were considered outliers by Francey et al. (1999a). They were the only DE08-2 samples analysed in 1995, and are considerably higher than the surrounding points (see Figure 3.24). These points were not included in the Kalman filter analysis already discussed. If they are included (averaged to give one data point at 1970), the sources change slightly between 1960 and 1980, with less ocean uptake and more biospheric uptake before 1970, and the opposite after 1970 (compare Figure 6.6b with Figure 5.17c, but note the different horizontal axis). The model doesn't actually fit this 1970 δ^{13}C value, the **Q** doesn't allow it, but it does drag the δ^{13}C curve up slightly (Figure 6.6a). To fit this point in the model would require extreme source changes. The reason for the high δ^{13}C relative to the surrounding points is not known, and sharp variation in the firn-smoothed δ^{13}C ice core record such as this is not expected. Again, new ice core measurements will be useful.

6.3 Natural variability

In this section, CO_2, δ^{13}C and the net fluxes from the forward, single and double deconvolution model calculations are compared with each other and with various forcing mechanisms. The focus here will be on natural variability on firstly the century then the decadal time scale. The anthropogenic perturbation will be discussed later.

6.3.1 Century time scale

Figure 6.7 shows CO_2, $\delta^{13}C$ and the net fluxes from the century-scale Kalman filter double deconvolution run, DD3. Also shown are two records of temperature variability over recent centuries – the Bradley and Jones (1993) northern hemisphere summer temperature anomaly record, based on tree ring, ice core and historical records, and the Mann et al. (1999) temperature reconstruction. Two forcing mechanisms that have been suggested as having some effect on climate in the pre-industrial period are solar forcing and volcanic eruptions (see Section 2.9.2). A record of solar irradiance from Rind et al. (1999) is shown, as well as the smoothed ^{14}C record from Eddy (1976). The Volcanic Explosivity Index (VEI) for many of the largest explosive volcanic eruptions since 1400, as given by Briffa et al. (1998) and taken from Simkin and Siebert (1994), is shown.

The deduced net CO_2 fluxes can be compared with variations in the likely forcings, although partitioning of the total CO_2 flux into oceanic and biospheric components in the pre-industrial needs to be treated with care, because the $\delta^{13}C$ data are rather sparse. The biospheric uptake between about 1500 and 1750 looks roughly like the Bradley and Jones (1993) northern hemisphere temperature record. After 1750 the biospheric flux becomes a source, and at least part (if not most) of this will have been due to land-use change. The lowest temperature in the Bradley and Jones record occurs between about 1560 and 1600, when CO_2 decreased to its lowest level for the last 1000 years. This is around the time of the Huaynaputina volcanic eruption. The Mann et al. (1999) temperature reconstruction is somewhat different, with the lowest temperature over the last 1000 years at about 1460, which is after the Kuwae eruption. The CO_2 measurement near 1460 is lower than nearby points, which may have been due to reduced temperatures. During 1800–1850, there was a large explosive volcanic eruption (Tambora in 1815, with a VEI of 7) as well as the Dalton Minimum in solar variability. These may have precipitated climate anomalies that contributed to the complicated behaviour of CO_2 and $\delta^{13}C$ between 1800 and 1850 described in the previous section.

Figure 6.8 shows CO_2, $\delta^{13}C$ and the net fluxes from the forward, single and double deconvolution calculations. The double deconvolution is the century time scale DD3 calculation. The forward and single calculations are exactly as has already been described in Chapter 4. By comparing these three calculations with the ice core records, some insight

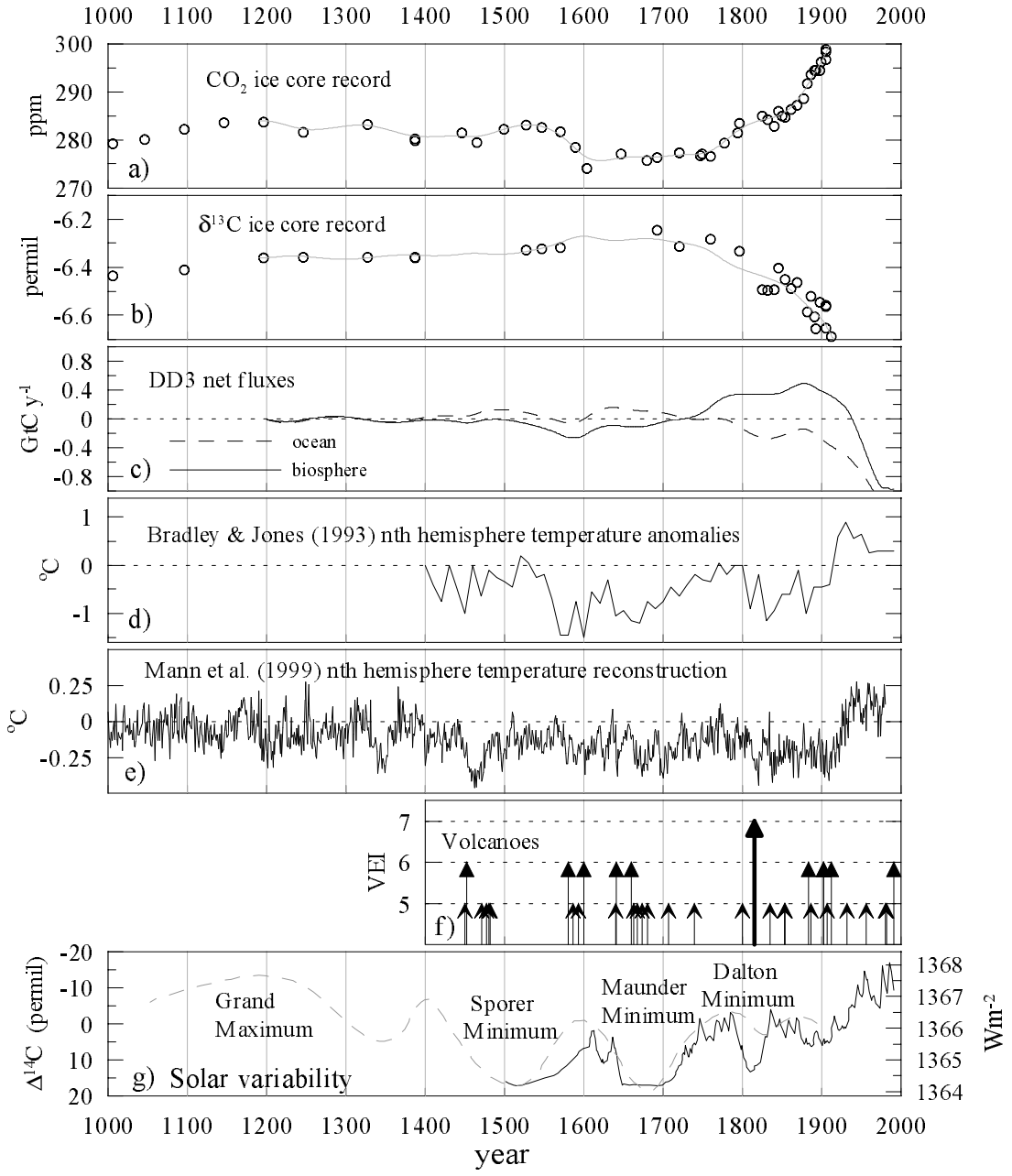

Figure 6.7: a) Law Dome CO_2 ice core record. b) Law Dome $\delta^{13}C$ ice core record. c) Net fluxes from the Kalman filter double deconvolution, DD3. d) Bradley and Jones (1993) northern hemisphere summer temperature anomalies. e) Mann et al. (1999) northern hemisphere temperature reconstruction. f) Volcanic Explosivity Index (VEI) for the largest explosive volcanic eruptions, from Briffa et al. (1998) and taken from Simkin and Siebert (1994). g) Solar irradiance reconstruction from Rind et al. (1999) (solid line, right axis) and the smoothed ^{14}C record from Eddy (1976) (dashed line, left axis).

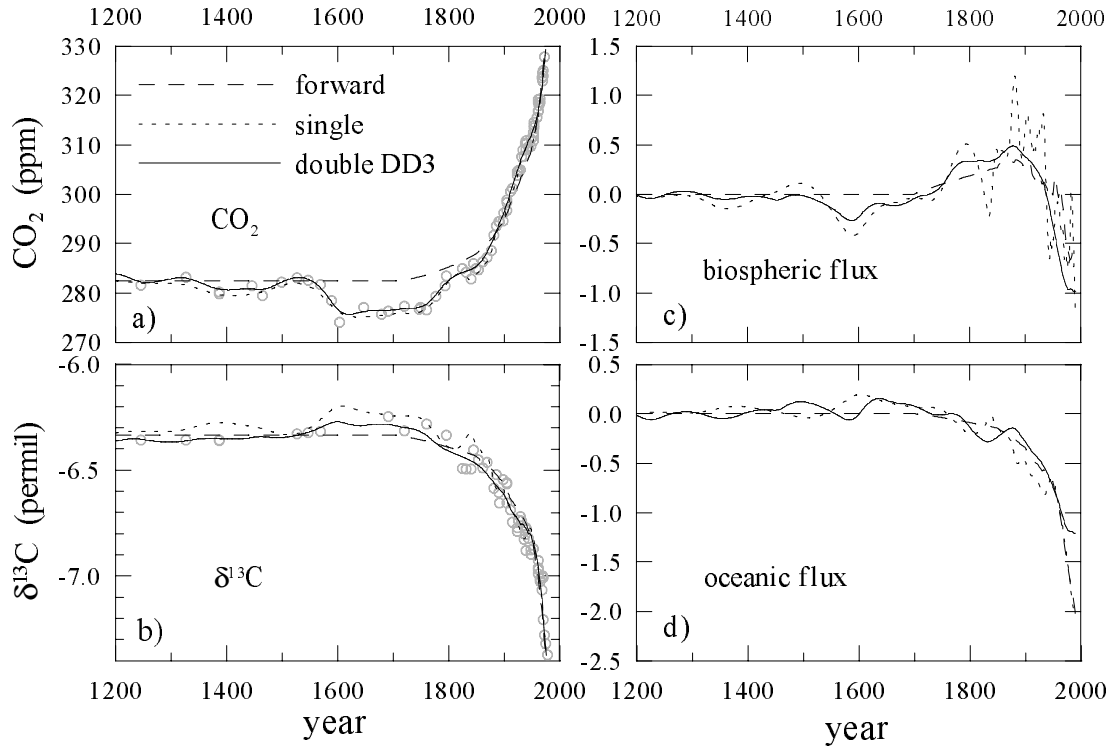

Figure 6.8: Results from the forward, single and double deconvolution calculations. The forward and single deconvolution calculations are exactly as described in Chapter 4. The double deconvolution is the century scale calculation, DD3.

can be gained into the effect of the fluxes on CO_2 and $\delta^{13}C$, and therefore the likely fluxes over the last 1000 years.

The LIA forward calculations in Chapter 4 suggested that the observed CO_2 and $\delta^{13}C$ were consistent with the response of the biosphere to reduced temperatures. The LIA forward calculations used a hypothetical temperature record of sustained cool temperatures between 1550 and 1800. This was chosen because the CO_2 during the LIA remained fairly steady at about 6 ppm lower than earlier levels, apart from the lowest point at 1604. The single and double deconvolutions do suggest biospheric uptake of CO_2 during this period, but not sustained uptake. They both have strongest biospheric uptake around 1600, and this is due to the CO_2 measurement dated 1604. A double deconvolution calculation without the 1604 CO_2 measurement doesn't have the dip in biospheric uptake around 1600 seen in DD3. Instead the biospheric uptake looks similar to the hypothetical temperature

record, but beginning and ending earlier (the sink occurs between 1500–1700 rather than 1550–1800). The model suggests that the CO_2 increase between about 1750 and 1800 (the LIA recovery) requires a source of CO_2, rather than just switching off a sink. This would be due to the fairly long 'lifetime' of CO_2 in the atmosphere.

The D57 CO_2 ice core record from Barnola et al. (1995), shown in Figure 2.8c, is somewhat different to the Law Dome CO_2 record in the pre-industrial period. The D57 record suggests that the lowest point over the last 1000 years was around 1200, and that there was a significant increase in CO_2 between 1200 and 1300. It is difficult to even comment on whether this may to have occurred instead of what is seen in the Law Dome record. The information on climate, volcanic eruptions and solar variability in Figure 6.7 for that time is too limited to give any additional insight.

6.3.2 Decadal time scale

Figure 6.9 shows the results of a Kalman filter double deconvolution calculation which uses the same **Q** and data uncertainties as DD1, but uses only DE08 and DE08-2 data (i.e. no DSS data) after 1830. This calculation will be known as DD1a. The DSS data are excluded (when there is good DE08/DE08-2 coverage) because, based on the firn model calculations in Section 3.7.1, DSS is probably more smoothed in time. It may be more confusing to use both DE08/DE08-2 and DSS data, unless a method for taking into account the different smoothing is used. Figure 6.9a shows the DE08 and DE08-2 CO_2 measurements (symbols), and the DD1a model fit to these measurements (line). Figure 6.9b shows $\delta^{13}C$ measurements and model fit. Figure 6.9c shows the total CO_2 flux (ocean + biosphere) from the Kalman filter double deconvolution, DD1a, minus the fluxes from the forward calculation from Chapter 4 (i.e. fossil fuel, land-use change, uptake due to fertilisation and modelled ocean uptake/release). This gives the contribution that is not already explained, and is presumably to a large extent due to climate variations. The uncertainties from the Kalman filter for the total flux are shown. Figure 6.9d shows the net biospheric and oceanic CO_2 fluxes from the double deconvolution, DD1a, minus the respective forward calculation fluxes. Also shown in Figure 6.9 is the Jones and Briffa (1992) global temperature record, and the Southern Oscillation Index data from http://www.dar.csiro.au/nino/SOItable.htm. The extended El Niño and La Niña events identified by Allan and D'Arrigo (1999) are indicated by the diamond symbols.

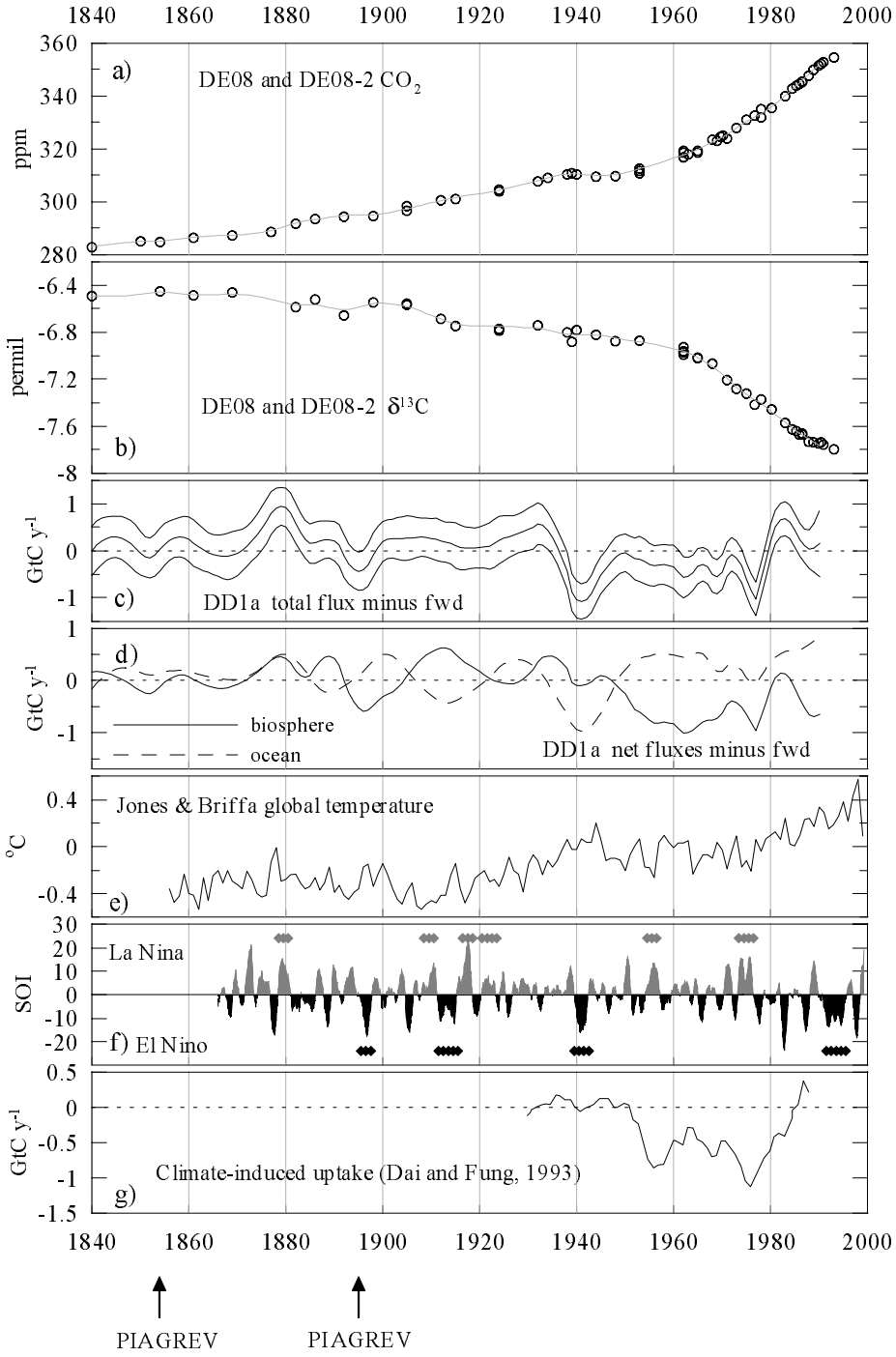

Figure 6.9: a) CO_2. b) $\delta^{13}C$. c) Total CO_2 fluxes (ocean + biosphere) minus the fluxes from the forward calculation. d) Oceanic and biospheric CO_2 fluxes. e) Global temperature from Jones and Briffa (1992). f) Southern Oscillation Index. g) Climate-induced biospheric uptake from Dai and Fung (1993). The two main episodes of the PIAGREV are also shown. (See text for details.)

Etheridge et al. (1996) noted that the persistent El Niño sequences identified by Allan and D'Arrigo (1999) around 1939–1943, 1895–1898 and 1911–1916 coincided with decreases in the CO_2 growth rate. The strongest of these growth rate decreases, the one around 1940, will be investigated in detail in the next section. The total flux (minus the forward fluxes) in Figure 6.9c does indicate low growth rates, particularly coinciding with the 1895–1898 and 1939–1943 extended El Niños. The longest El Niño sequence between 1911–1916 has no growth rate decrease. The data density may not be quite high enough to show the flattening if it did occur. Another CO_2 measurement for 1920 might indicate whether there was also a growth rate decrease for this El Niño sequence. In addition this sequence is between two of the extended La Niña sequences, and if the response of CO_2 to La Niña is opposite to that of El Niño, the 3 events may be smeared in the ice core record by firn smoothing. The double deconvolution has partitioned the net fluxes into biospheric and oceanic exchange as shown in Figure 6.9d. The 1895–1898 uptake seems to be due to the biosphere, and the 1939–1943 uptake due to the ocean. The $\delta^{13}C$ measurements may not be precise enough to identify with certainty whether biospheric or oceanic fluxes are responsible for the flattening.

Langenfelds et al. (in prep) are investigating the relationship between CO_2 and the SOI on interannual time scales. They detect an increase in the CO_2 growth rate during El Niño events, rather than the decrease that is seen in the ice core records. It is likely that different mechanisms are important for determining the response of CO_2 to ENSO on different time scales. The Rayner et al. (1999b) study into CO_2 and ENSO (mentioned in Section 2.9.3) found an initial reduction of the tropical ocean source, later offset by increased CO_2 release from land. This land release may be due to biomass burning of dried out vegetation, and after fuel stocks are depleted, the reduced source due to upwelling may again dominate. The effect of ENSO on CO_2 is complicated as it involves both oceanic and terrestrial processes on a range of time scales. The time resolution of ice core measurements from the DE08 site should be sufficient to give useful insight into the effect of SOI on CO_2 fluxes for the extended El Niño sequences. However, the sampling density and precision of the Law Dome record at present is too low to make firm conclusions about SOI and CO_2.

It was suggested by Holdsworth et al. (1996) that increased biomass burning known as the PIAGREV occurred between 1850 and 1900, with 2 main episodes between 1850–1860

and 1890–1900. The suggested timing of the two main episodes is indicated in Figure 6.9, but there is no strong indication in the fluxes of peaks at these times. The Houghton land-use change estimates are part of the forward calculation fluxes subtracted from the double deconvolution fluxes, and they also show no evidence of such peaks (Figure 2.12b). The double deconvolution has biospheric peaks centered around 1880 and 1890, but it is possible that these are driven by individual δ^{13}C measurements, and further confirmation would be needed.

The net CO_2 flux due to climate variations (temperature and precipitation) calculated by Dai and Fung (1993) is shown in Figure 6.9g. The temporal evolution and magnitude of this flux is similar to the net terrestrial flux from the double deconvolution DD1a in Figure 6.9d. Dai and Fung compared their flux to the missing sink derived by single deconvolution to the Siple CO_2 record by Houghton (1989). The climate-induced sink reduced to about 0.5 GtC y^{-1} during the 1960s, while the Houghton (1989) deconvolution sink increased slowly through this period. The DD1a double deconvolution terrestrial sink also decreases to about 0.5 GtC y^{-1}, but in the early 1970s, which is later than the climate-induced sink. The data gap of 9 years in the DE08/DE08-2 measurements leading up to the early 1960s will limit the ability of the model to determine the fluxes accurately. The terrestrial flux in DD1a around 1977 agrees very well with the Dai and Fung uptake. Due to firn smoothing, the flux reconstructed from ice core measurements couldn't be expected to have as much temporal structure as that calculated by Dai and Fung, and the calculation using Siple data is expected to have smoother flux variation than that using DE08/DE08-2 data. The Jones and Briffa (1992) temperature record in Figure 6.9e doesn't have the same temperature evolution as the climate-induced flux. This shows the need to take into account the spatial distribution of temperature and how this affects the spatially distributed CO_2 fluxes to determine variations in global levels.

Joos et al. (1999) found that natural variations in the net fluxes were usually less than ± 0.2 GtC yr^{-1} on time scales of decades to centuries. This is dependent on the degree of smoothing they have used. Their CO_2 and δ^{13}C splines through the industrial period didn't fit a number of the features that have been assumed by the KFDD to be real. Their δ^{13}C spline is much smoother than is suggested by the δ^{13}C measurements with the uncertainties assigned by Francey et al. (1999a). The DD1a calculation suggests that

natural variations in the net fluxes may be as large as ± 1 GtC yr^{-1} on time scales of perhaps slightly less than a decade up to centuries. The DD2 calculation has smaller variability, but still greater than that in Joos et al. These conclusions depend strongly on the data uncertainties and what variability in CO_2 and $\delta^{13}C$ is taken as real. The variability that will be seen by analysing ice core measurements depends on the firn smoothing and what features are stored in ice. The calculations presented here assume that many of the decadal time scale features represent real atmospheric changes. The firn model has shown that features such as these can survive firn smoothing. It remains to be tested (by new ice core measurements) which of the features are real.

Figure 6.10 shows $\delta^{13}C$ versus CO_2 for the double deconvolution DD1a. The ice core measurements are also shown. This double deconvolution calculation closely fits many of the features in both the CO_2 and $\delta^{13}C$ records, so there is good agreement between the model and observations is this figure. However, there is less of a sense of a series of 'steps' in the $\delta^{13}C$ decrease, as was suggested by Francey et al. (1999a) for the splines in Figure 4.12. The decadal variations in $\delta^{13}C$ in the double deconvolution are mainly attributed to net fluxes rather than the isofluxes, and the net fluxes deduced by DD1a are shown in Figure 6.9d. It is still possible that if decadal variations in the isofluxes are large (this work has assumed that they are not) that some of the $\delta^{13}C$ features are partly due to isofluxes rather than net fluxes. However, the fact that the magnitude and timing of the deduced biospheric flux after 1940 agrees so well with the Dai and Fung (1993) climate-induced flux gives confidence that variations in the biospheric net flux of up to about 1 GtC yr^{-1} on the decadal time scale can explain much of the variation in $\delta^{13}C$.

6.4 The 1940s flattening

The flattening in the DE08/DE08-2 CO_2 record around 1940 is a very prominent feature in the CO_2 variation over the 20th century. The ice core measurements themselves suggest that atmospheric CO_2 concentration actually decreased for a few years, despite the continued input of CO_2 from fossil fuel burning and land-use change. And, due to the smoothing in the firn, the real atmospheric CO_2 variations were probably even more extreme than the ice core measurements show. It will be accepted here that the DE08 and DE08-2 ice core measurements provide an accurate, but smoothed, representation of

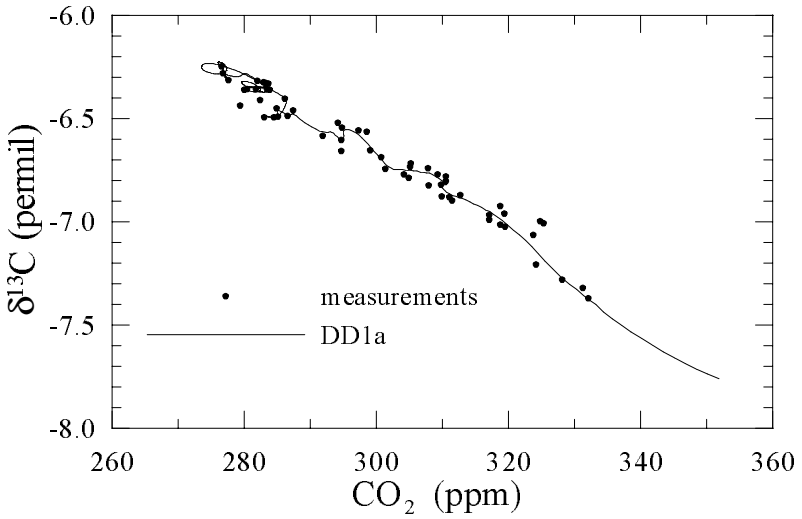

Figure 6.10: δ^{13}C versus CO_2. The line shows the results from the double deconvolution calculation, DD1a.

atmospheric CO_2, and are not influenced by contamination. Implications of the CO_2 and δ^{13}C records for net CO_2 fluxes will be studied. Some discussion was given in Section 3.7.1 of the smoothing due to the firn processes. This will be summarised, then results from the forward, single and double deconvolution calculations around this time compared to deduce the fluxes that are consistent with the CO_2 and δ^{13}C measurements. A preliminary analysis of decadal time scale variations over the 20^{th} century in sea surface temperature is then explored.

6.4.1 Actual and reconstructed variations

Figure 3.16 in Section 3.7.1 shows the calculated trapped CO_2 profiles at DE08/DE08-2 for 3 different atmospheric CO_2 histories. The histories that give a trapped profile in the model similar to observed have a peak in the early 1940s and a trough around the late 1940s or 1950 (RUN2 and RUN3). RUN3 involves a significant decrease in atmospheric CO_2 of around 5 ppm over about 7-8 years at a time when fossil fuel was contributing about 1.3 GtC (0.6 ppm) per year to the atmosphere. RUN2 gives a larger CO_2 decrease over a shorter time.

The $^{14}CO_2$ bomb pulse trapped in ice was used to test the smoothing of the diffusion and trapping processes in the firn model. Unfortunately there are some uncertainties

in $\Delta^{14}C$ due to the incomplete understanding of *in situ* produced ^{14}C, particularly at low accumulation rate sites. Until the contribution of *in situ* produced ^{14}C is better understood, measurements of bomb ^{14}C in ice and firn should be used with some caution.

The firn model gives fairly good agreement with DE08/DE08-2 firn and ice $\Delta^{14}C$, although the modelled peak is lower than observations, possibly indicating that the model is slightly over-smoothing for DE08. The *in situ* production at DE08 is expected to be small, but if there is some contribution of *in situ* produced ^{14}C in the air bubbles it would improve the agreement of the model and observations.

The CO_2 flattening at DE08/DE08-2 is not seen in the DSS, Siple or H15 ice core measurements (Figures 3.14b and 3.15). This is probably due to the lower time resolution of these cores. The firn model for DSS with diffusivity and accumulation rate tuned by V. Levchenko for the ^{14}C measurements does suggest greater smoothing at DSS than DE08 (18–20 years at DSS compared with 11.5 years at DE08, see Chapter 3), but not quite enough that the flattening is expected to disappear completely. Information on DSS is scarce, particularly as there are no firn air measurements. The most useful information for DSS is the mean age of trapped air from CO_2 or CH_4 measurements and smoothing from the ^{14}C bomb pulse, except that again ^{14}C has large uncertainties due to *in situ* produced ^{14}C. From the information available it seems likely that the greater smoothing at DSS explains the lack of CO_2 feature in DSS ice, rather than it contradicting the DE08/DE08-2 record (see Section 3.7.1).

The preliminary DSSW20K firn CO_2 measurements are not able to help much here. The smoothing given by the firn model for DSSW20K is such that the pulse should probably be seen in the firn measurements. However, as discussed in Section 3.8, it was not possible to match with the model the 2 deepest CO_2 and SF_6 measurements. The RUN3 atmospheric record was used in the model, and the agreement with the CO_2 measurements was even worse than with the standard spline atmospheric input.

6.4.2 Fluxes

Some understanding of CO_2 in the 1940s can be gained by looking closely at the results of the forward, single and double deconvolution calculations already described. The double deconvolution suggests ocean uptake is responsible for the CO_2 decrease (Figure 6.9d), as does the analysis by Joos et al. (1999). The CO_2 from the forward calculation in Chapter 4

(Figure 4.3a), with fossil fuel, land-use change and fertilisation, shows no evidence of the CO_2 pulse. As already pointed out, the modelled CO_2 is lower than observations after 1900 and until about 1950, which is at the end of the CO_2 flat period, when the model rejoins the observations. Modelled $\delta^{13}C$ is higher than the $\delta^{13}C$ measurements during this period. The CO_2 in the single deconvolution from Chapter 4 follows a spline fit to measurements from all 3 Law Dome ice cores, and the CO_2 growth rate decreases to zero but doesn't actually go negative. With this CO_2 record, the rate of change of $\delta^{13}C$ changes sign around 1943 and increases until about 1950 (Figure 4.10b). The response of the $\delta^{13}C$ is stronger than that of CO_2. $\delta^{13}C$ from the single deconvolution, which attributes the flattening to the biosphere, doesn't appear consistent with the DE08 and DE08-2 $\delta^{13}C$ measurements.

Firn smoothing will have had an effect on both the CO_2 and $\delta^{13}C$ in the ice core record compared with the atmospheric variations. The response of atmospheric $\delta^{13}C$ to a biospheric flux is stronger than that of CO_2, but firn smoothing will treat them differently. The single deconvolution calculation uses a fit to all of the Law Dome CO_2 measurements (i.e. including DSS), while the firn model calculations suggested that a more extreme feature than is seen in the DE08/DE08-2 record may have occurred. The single deconvolution calculation was run with the RUN3 CO_2 record between 1930 and 1960 instead of the standard spline (with the standard spline before and after). $\delta^{13}C$ given by the BDM is shown in Figure 6.11a (solid line). The firn model was then run with the CO_2 and $\delta^{13}C$ from the BDM and the calculated trapped $\delta^{13}C$ is shown by the dotted line in Figure 6.11a. (The trapped CO_2 agrees with the DE08/DE08-2 CO_2 measurements, by design.) Compared to the solid line, the pulse shown by the dashed line appears earlier in the record, and is smoothed. As with the standard single deconvolution output, this $\delta^{13}C$ record does not seem consistent with the Law Dome $\delta^{13}C$ measurements, although the differences are not large. Figures 6.11b and 6.11c show the biospheric and oceanic fluxes from the standard single deconvolution calculation in Chapter 4 (dashed line) and the one with RUN3 CO_2 variation (solid line). The model requires a biospheric uptake of about 3 GtC y^{-1} for a few years to match the RUN3 CO_2 record.

Two double deconvolution calculations using a series of CO_2 'data' that define the RUN3 CO_2 record are shown in Figure 6.12. The plots on the left show the results

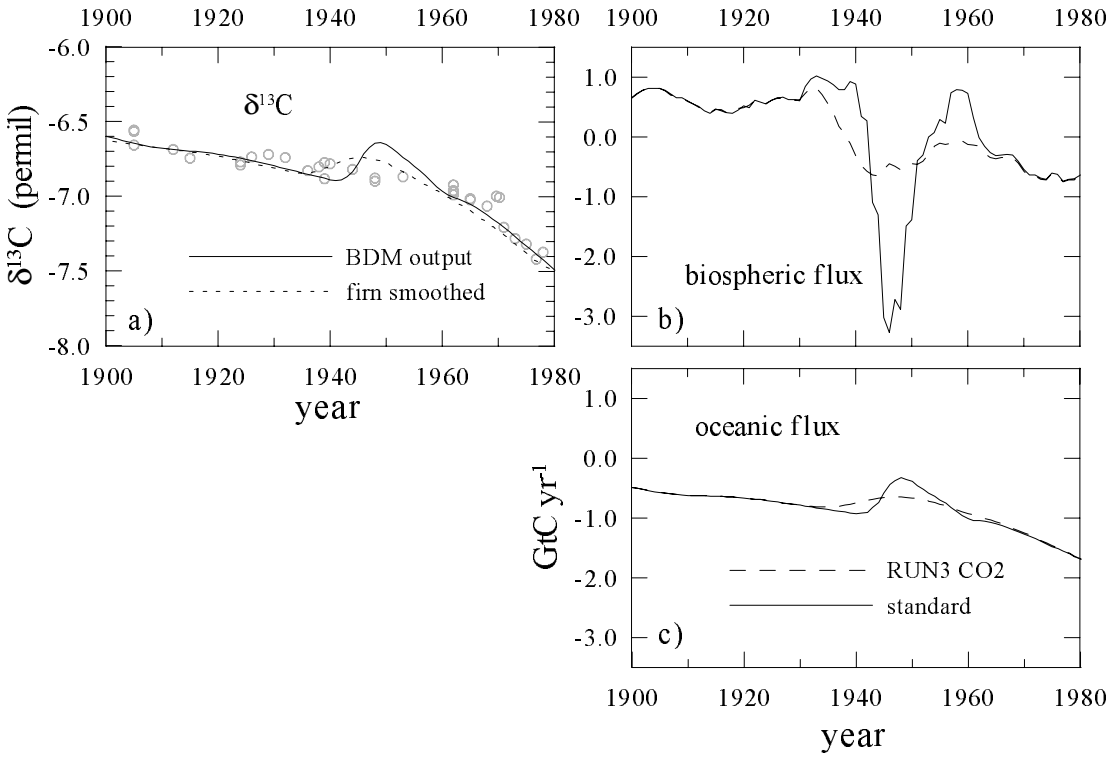

Figure 6.11: a) Solid line shows the δ^{13}C calculated by the single deconvolution with the RUN3 CO_2 curve. The dotted line shows this record smoothed by the firn model. b) The solid line shows the biospheric fluxes estimated by the single deconvolution with the RUN3 CO_2 record, and the dashed line shows the flux from the standard single deconvolution. c) Oceanic flux from the single deconvolution with RUN3 CO_2 record (solid line) and the standard calculation (dashed line).

calculated using the published δ^{13}C uncertainties and on the right using 4 times the published δ^{13}C uncertainties. CO_2 uncertainties of 0.6 ppm were used in both cases. With the small δ^{13}C uncertainties the model attributes the additional uptake to the ocean, and requires about 2.5 GtC y^{-1} ocean uptake in the mid 1940s. With the large δ^{13}C uncertainties the model allows just less than 2 GtC y^{-1} ocean uptake and about 1 GtC y^{-1} biospheric uptake in the mid 1940s. The second case has a peak in atmospheric δ^{13}C around 1950, but this disappears completely with firn smoothing. From these calculations, the CO_2 and δ^{13}C data are consistent with strong CO_2 uptake in the 1940s that is at least two thirds due to the oceans. It may be totally due to oceanic uptake, or up to about one third biospheric uptake. The Dai and Fung (1993) climate-induced net terrestrial flux shows no evidence of biospheric uptake in the 1940s, suggesting that it may in fact have

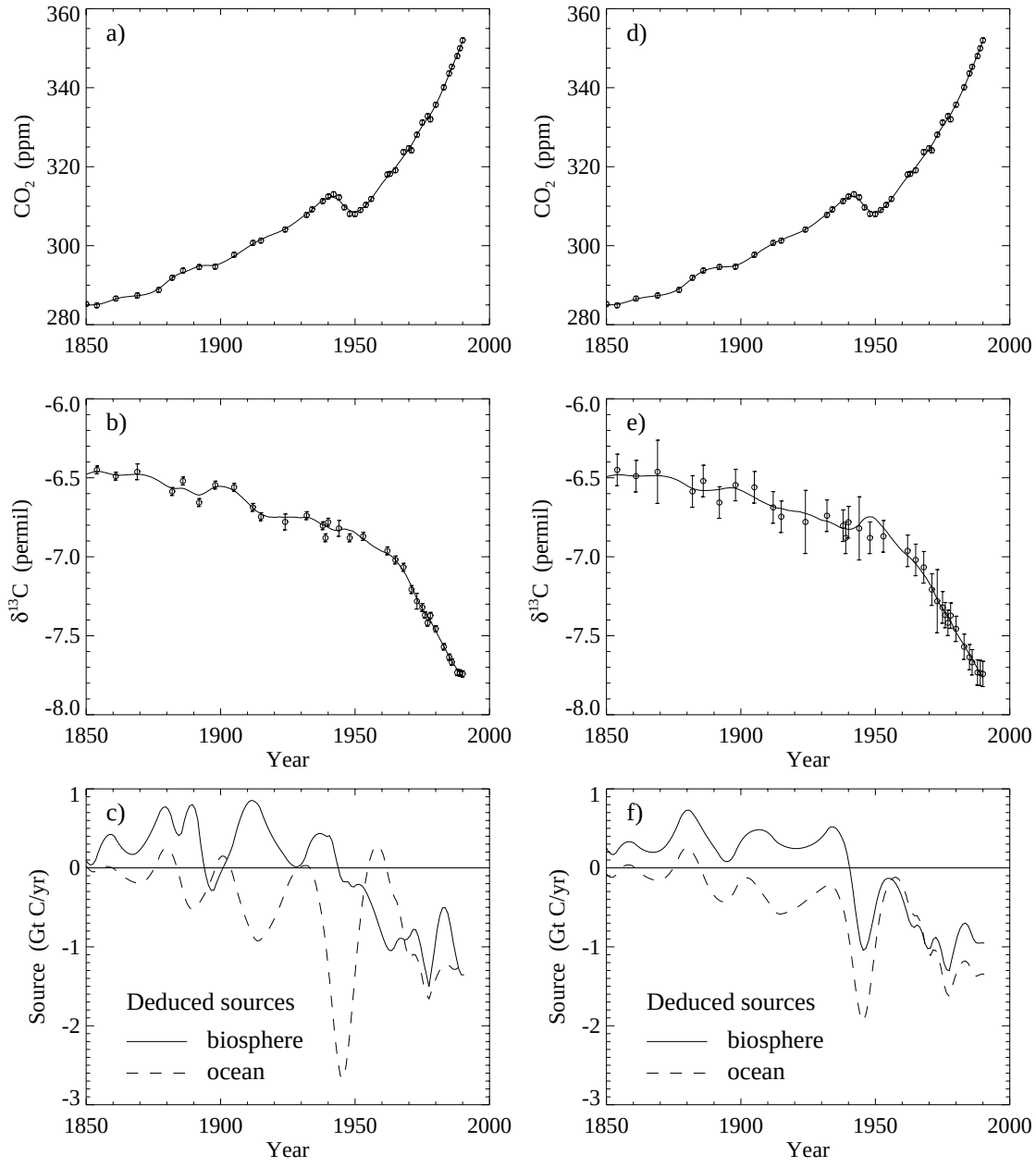

Figure 6.12: Double deconvolution results for CO_2 variation given by the RUN3 record. a), b) and c) show the case using published δ^{13}C uncertainties and d), e) and f) show that using 4 times the published δ^{13}C uncertainties.

been mostly oceanic.

These calculations have determined fluxes that are consistent with the firn diffusion model and the box diffusion carbon cycle model, and the DE08/DE08-2 CO_2 and $\delta^{13}C$ ice core measurements around 1940. It still remains to find processes that can explain the large fluxes required.

6.4.3 Climate

Climate around 1940 was unusual for a number of reasons. As already discussed, the period 1939–1942 was one of the persistent El Niño events identified by Allan and D'Arrigo (1999). ENSO is an interannual phenomenon. The patterns of global sea surface temperature on the interdecadal time scale are also interesting, and are perhaps more relevant for CO_2 variations seen in the ice core record. A number of recent studies have performed EOF analysis on the global SST field. Some results of this work, and possible relevance to the carbon cycle are discussed here, suggesting one way that analysis of the CO_2 ice core records may proceed.

A dominant EOF mode on the interdecadal time scale with a spatial pattern similar to that of ENSO has been identified (Zhang et al., 1997; Power et al., 1999; Cai et al., 2001). This ENSO-like mode, also called the Interdecadal Pacific Oscillation (IPO) by Power et al. (1999), is less equatorially confined in the Eastern Pacific and more prominent in the extra tropical North Pacific than ENSO. The IPO is a background condition, around which the interannual ENSO variations take place. Power et al. (1999) found that when the IPO is negative (i.e. cool temperatures in the tropical Pacific Ocean), there is a strong relationship between year-to-year ENSO variability and year-to-year climate variations in Australia. When the IPO is positive, this relationship breaks down. Cai et al. (2001) found that not only was this the case with Australian climate, but that the relationship between ENSO and global rainfall also depends on the sign of the IPO. The IPO was low around 1940, and the correlation between ENSO and global mean SST (shown in Figure 6.13) was weak. Cai et al. (2001) found that during the period 1930–1945, the SOI and the Northern Atlantic Oscillation (NAO) are correlated, whereas the correlation for 1889–1999 is virtually zero. They suggested that the correlation of ENSO and global mean SST broke down in this period because the covarying northern high latitude variability took over as the mode influencing interannual fluctuations for global mean SST. This may

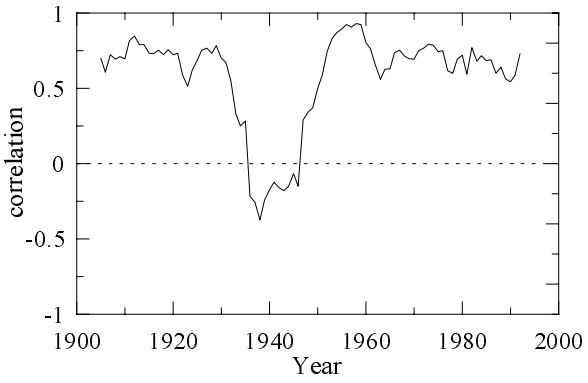

Figure 6.13: Correlation between ENSO and global mean SST from Cai et al. (2001).

have implications for atmospheric CO_2. Further analysis of the SST variations and how they may be related to changes in CO_2 fluxes might give some insight into the 1940s CO_2 anomaly.

The EOF analysis by Cai and Whetton (2001) identified 3 multidecadal (> 15 years) modes – a trend mode, the ENSO-like mode and what they call the North Atlantic-North Pacific (NANP) mode. The NANP mode has maximum weights in the North Atlantic and eastern midlatitude Pacific. W. Cai (pers. comm., 2000) repeated the EOF analysis to determine the dominant modes for time scales of greater than 10 years. Figure 6.14 shows the spatial patterns of the three leading EOFs, which are very similar to the modes for time scales longer than 15 years in Cai and Whetton (2001). Figure 6.15 shows the time series of the SST anomalies attributable to the ENSO-like EOF (dotted line) and the NANP EOF (dashed line). Also shown is the time series of global mean SST anomalies on time scales longer than 10 years minus the trend mode EOF (first EOF). These EOF time series are scaled so that they show the contributions of each EOF to the global temperature variation.

These SST patterns and their variations may be relevant to the carbon cycle if they correspond to regions where there are significant natural or anthropogenic CO_2 fluxes, and if the temperature variations either cause or are a sign of changes in processes that affect CO_2 exchange. ENSO has an effect on CO_2 fluxes in the tropical Pacific ocean, and it is possible that the IPO will be related to variations in CO_2 flux on the decadal time scale. The NANP mode shows variations in the North Pacific ocean, which is a region of strong

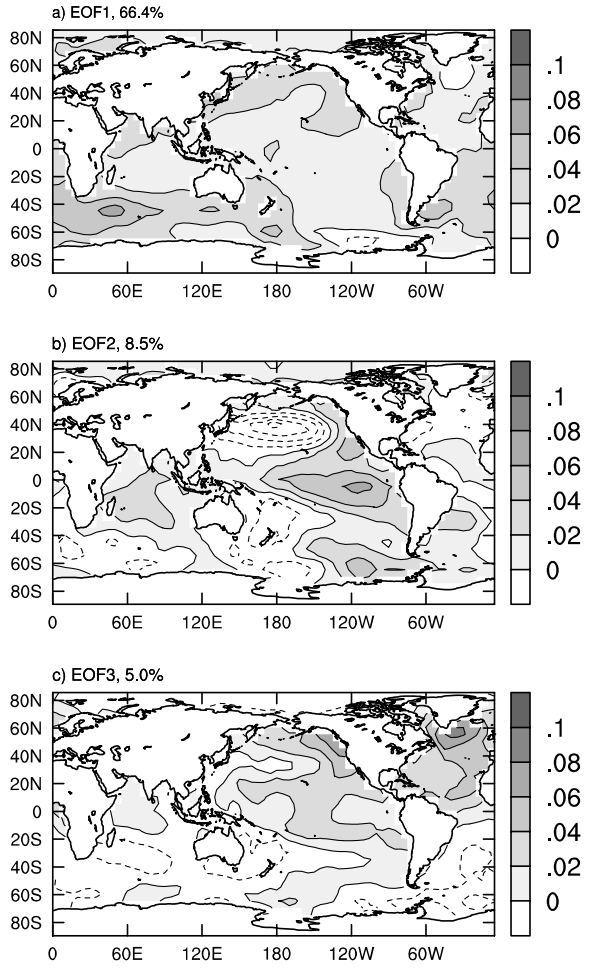

Figure 6.14: Spatial patterns of the 3 leading EOFs from the analysis of SST data by W. Cai (pers. comm., 2000).

CO_2 uptake.

The time series in Figure 6.15 show no particular behaviour in the 1940s that may suggest a cause for the large ocean uptake described in the previous section. It may be possible to analyse the variability of spatial SST patterns that are more directly related to CO_2 flux distributions, and this may give better results. This type of analysis for the oceans may be useful in the same way as the Dai and Fung study for the biosphere.

6.5 Anthropogenic trend

The overall decrease in $\delta^{13}C$ from pre-industrial to modern-day levels depends on both the net CO_2 fluxes and the isofluxes. In a double deconvolution with isofluxes determined

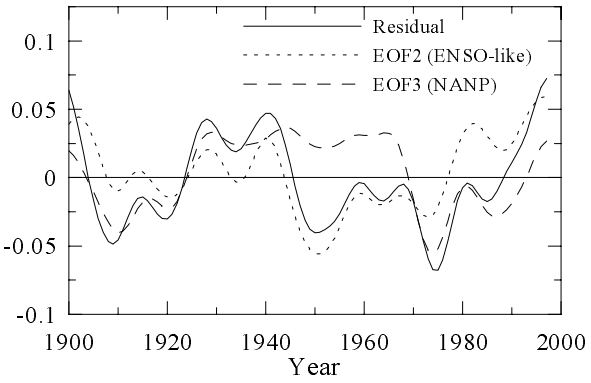

Figure 6.15: The dotted and dashed lines show the time series associated with the ENSO-like and NANP EOFs, respectively. The solid line shows the time series of global mean SST minus the trend mode EOF.

with ocean and biosphere models, the δ^{13}C change acts as a constraint on partitioning the net uptake of anthropogenic CO_2. Thus, how well the pre-industrial – modern δ^{13}C change is known is important. The uncertainty on the decadal variability of the net fluxes deduced using decadal variations in CO_2 and δ^{13}C is different to the uncertainty on the longer term partitioning, and depends on different things.

In Chapter 3, a discrepancy between the South Pole firn δ^{13}C record and the Law Dome ice core record was discussed. The reasons for this discrepancy are not currently known. It is likely that one of these two records has some problem that causes an increasing offset with depth/age, and new measurements of δ^{13}C from firn and ice are needed to solve this. Until this is done, it is possible to quantify how much difference this uncertainty in δ^{13}C makes to the deduced net CO_2 fluxes.

Figure 6.16 shows a double deconvolution calculation that uses a δ^{13}C record created by decreasing the Law Dome δ^{13}C measurements by an amount that increases back in time between 1974 and 1900 to agree with the South Pole firn record. Before 1900 these δ^{13}C data are 0.2 ‰ lower than the Law Dome measurements. This double deconvolution calculation uses the same uncertainties as, and is compared to, the standard DD2 calculation. The total isoflux in 1990 is about 8 GtC ‰ y^{-1} (10 %) smaller with the smaller South Pole δ^{13}C decrease compared to with the Law Dome decrease. The biospheric uptake is about 0.5 GtC y^{-1} larger, and the oceanic uptake about 0.5 GtC y^{-1} smaller, for the South Pole δ^{13}C decrease. After 1974 the same δ^{13}C measurements are used in the calculation, so the

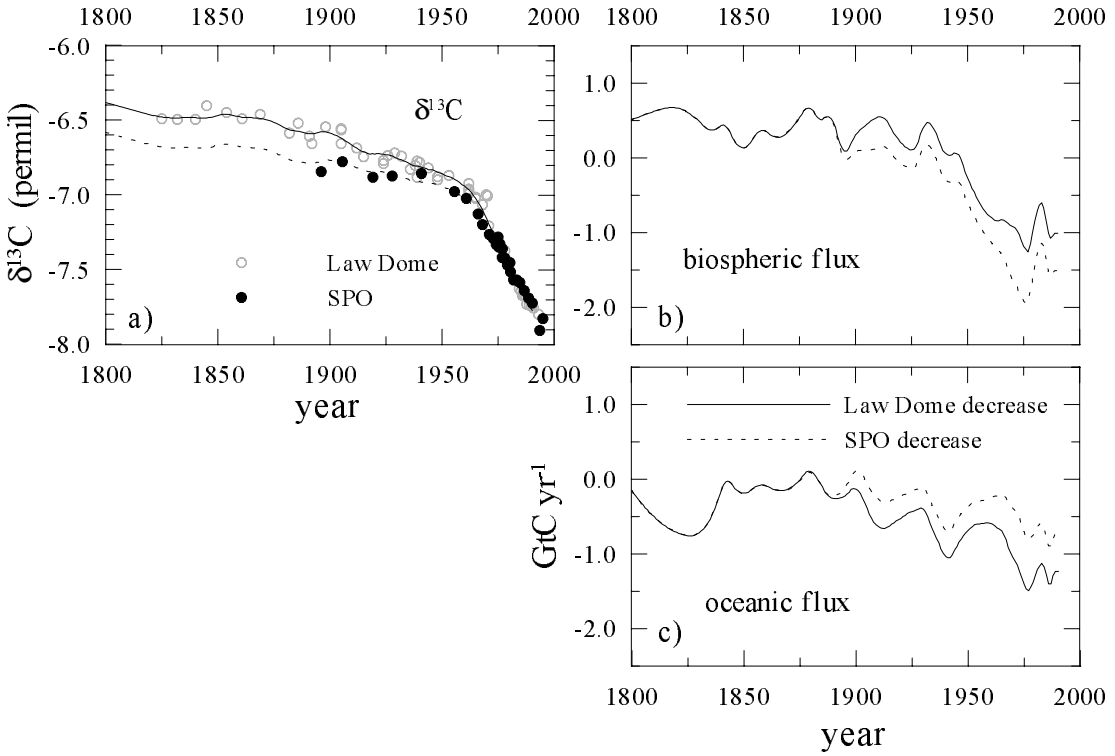

Figure 6.16: The solid lines show the DD2 double deconvolution results. The dashed lines show the results of a double deconvolution calculation that uses the Law Dome δ^{13}C ice core measurements decreased so that they agree with the South Pole firn measurements (solid symbols).

difference in the flux partition after 1974 is due to the different isofluxes. Between 1900 and 1974 the partitioning for the shifted record would differ due to the slightly different atmospheric rate of change of δ^{13}C, as well as due to the isofluxes.

The difference the smaller δ^{13}C decrease makes to the partitioning is similar to the uncertainty due to calculating the isoflux with different ocean models as described in Section 6.1. With new firn and ice core measurements that address some of the concerns described in Chapter 3 for the Law Dome ice core and South Pole firn measurements, it should be possible to substantially reduce the uncertainty on the δ^{13}C decrease so that it becomes a strong constraint on partitioning.

6.6 Concluding remarks

This chapter began with discussion of the isofluxes that are required for ^{13}C budgeting. Many of the recent estimates of terrestrial, ocean and total isofluxes were compared. As Thompson and Randerson (1999) pointed out, calculated isofluxes have significant interannual variability because atmospheric variations on the interannual time scale are not mirrored in the ocean or terrestrial biosphere. This can lead to interannual variations in the flux partitioning of up to about 0.4 GtG y^{-1}, which is small compared to variations in the net biospheric flux but may be important for the oceanic flux. Variation in the calculated ocean isoflux due to using different ocean models corresponds to a difference in the net flux partition of about 0.8 GtG y^{-1} in 1990. Calculations with a simple one box biosphere model showed that the isotopic disequilibrium is sensitive to the turnover time of the reservoir, which is affected by both the gross flux and the reservoir size. The isoflux, because it is the product of the gross flux and the disequilibrium, is less sensitive to the gross flux than to the reservoir size.

The double deconvolution results were discussed and compared with a number of indicators of climate or drivers of climate. There is some evidence of a decrease in the atmospheric growth rate of CO_2 coinciding with the extended El Niño events identified by Allan and D'Arrigo (1999). However there are not enough $\delta^{13}C$ points to make firm conclusions about these events. An important result is that there is very good agreement with the biospheric flux from the double deconvolution and the climate-induced flux estimated by Dai and Fung (1993). The double deconvolution calculation, DD1a, with the published $\delta^{13}C$ uncertainties and reduced CO_2 uncertainties suggests that natural variations in CO_2 net fluxes may be as large as 1 GtC y^{-1} on time scales of slightly less than decades. This is higher than the estimate by Joos et al. (1999) using the same ice core record, and this result depends very much on the smoothing and data uncertainties that are used. The DD1a calculation pushes the ice core data to its limits, and really needs confirmation of the variation in the records from new ice core measurements.

The behaviour of CO_2 during the 1940s was investigated in detail. Atmospheric variations consistent with the CO_2 measurements and the firn model require almost 3 GtC y^{-1} uptake of CO_2 in the mid 1940s. The $\delta^{13}C$ measurements suggest this is mostly oceanic, but may be up to about one third biospheric. A preliminary look at decadal time scale

variations in sea surface temperature patterns failed to shed any light on causes of this uptake. The correlation between ENSO and global mean SST reverses sign in the period roughly 1935–1945. This needs further analysis to determine whether it might be related to the 1940s CO_2 anomaly.

Finally, the sensitivity to the change in $\delta^{13}C$ from pre-industrial to modern levels was investigated. The net flux partitioning changed by 0.5 GtC y^{-1} for the $\delta^{13}C$ decrease in the South Pole firn record compared to that from the Law Dome record.